Borehole Microseismic Imaging of Hydraulic Fracturing: A Pilot Study on a Coal Bed Methane Reservoir in Indonesia

Rexha Verdhora Ry[1,*], Tepy Septyana[2], Sri Widiyantoro[1], Andri Dian Nugraha[1] & Arii Ardjuna[3]

[1]Global Geophysics Research Group, Faculty of Mining and Petroleum Engineering, Institut Teknologi Bandung, Jalan Ganesha No 10, Bandung 40132, Indonesia
[2]BP Indonesia, Jalan Letjen TB Simatupang Kav 88, Jakarta, Indonesia, 12520
[3]SKK Migas, Jalan Gatot Subroto Kav 42, Jakarta, Indonesia, 12710
*E-mail: rexha.vry@gmail.com

Abstract. Over the last decade, microseismic monitoring has emerged as a considerable and capable technology for imaging stimulated hydraulic fractures in the development of unconventional hydrocarbon resources. In this study, pilot hydraulic-fracturing treatments were operated at a coal-bed methane (CBM) field in Indonesia to stimulate the flow and increase the reservoir's permeability while the monitoring system was set in a single near-vertical borehole. Locating event sources accurately is fundamental to investigating the induced fractures, but the geometry of a single downhole array is a challenging data processing task, especially to remove ambiguity of the source locations. The locating procedure was reviewed in 3 main steps: (i) accurate picking of P- and S-wave phases; (ii) inclusion of P-wave particle motion to estimate the back azimuth; (iii) guided inversion for hypocenter determination. Furthermore, the seismic-source moment magnitudes were calculated by employing Brune's model. Reliable solutions of locations were obtained as shown statistically by uncertainty ellipsoids and a small misfit. Based on our results, both induced and triggered seismicity could be observed during the treatments and therefore conducting intensive monitoring is important. The triggered seismicity is an undesired activity so disaster precautions need to be taken, in particular for preventing reactivation of pre-existing faults.

Keywords: *downhole receivers; fracture stimulation; induced seismicity; microseismic; CBM; unconventional hydrocarbon.*

1 Introduction

The utilization of unconventional hydrocarbon resources has become a new hope for actualizing national energy security in Indonesia. Learning from other countries, North America in the past decade has been successful in utilizing unconventional resources and changed its domestic energy landscape by becoming a pioneer in shale gas exploration and exploitation (see e.g. Maxwell [1]). The main challenge of the exploitation of unconventional reservoirs such

Received September 24th, 2018, Revised January 31st, 2019, Accepted for publication March 19th, 2019.
 ISSN: 2337-5779, DOI: 10.5614/j.eng.technol.sci.2019.51.2.7

as CBM is that the reservoirs are tight and intrinsically impermeable. Hydraulic fracture treatment must be applied to unlock unconventional reservoirs to stimulate flow and create hydraulically conductive pathways in the rocks.

With this recent industry focus and the associated requirement for the effective treatment of hydraulic fracturing, microseismic monitoring has developed into a robust technology in the geophysical community. In microseismic monitoring, acoustic emissions caused by natural or artificially induced sources below the surface are recorded passively. The event source, also frequently referred to as microseismic event, has a minuscule magnitude and is associated with inelastic geomechanical fracture deformation. Maxwell [1] notes that by monitoring microseismicity, particularly in hydraulic-fracturing treatment, stimulated fractures can be imaged effectively and thus provide important geomechanical parameters of the reservoir.

In Indonesia, microseismic monitoring has been undertaken in many fields especially for geothermal exploration (Stimac, *et al*. [2], Akbar, *et al*. [3], Nugraha, *et al*. [4], Hasanah, *et al*. [5], Ry & Nugraha [6], Fattah, *et al*. [7], Rohaman, *et al*. [8], Palgunadi, *et al*. [9]). Typically, passive recording stations are deployed on the surface. The daily routine of this monitoring is to constrain the microseismic distribution and source attributes. Determination of the source locations mostly uses methods that minimize the difference between the observed and calculated arrival times for both P- and S-waves at the monitoring stations through an assumed velocity model (Geiger [10], Lienert, *et al*. [11], Nelson & Vidale [12], Lomax, *et al*. [13], Ry & Nugraha [14]). With regard to this, Pavlis [15] states that the geometry of the monitoring array, the velocity model, and errors in first arrival time picks determine the location accuracy.

For our case study, hydraulic-fracturing treatments were carried out at a coal-bed methane (CBM) field in August 2012. As a pilot project, the development of this unconventional resource focused on stimulating the flow and increasing the permeability of the reservoir. For monitoring, eight geophones were installed almost vertically in a single downhole, as utilized widely in the monitoring of fractures induced by hydraulic fracturing. Locating event sources accurately is fundamental to investigation of induced fractures. Downhole geometry analysis may detect small fractures more sensitively and better constrains their depth. However, this technique suffers from ambiguities in the horizontal plane due to the distribution of the misfit function and consequently requires a more challenging data processing task. Here, additional information on P-waves particle motion is necessary for limiting the back azimuth from the receiver to the event source (Alessandrini, *et al*. [16], Moriya [17], de Meersman, *et al*. [18], Maxwell, *et al*. [19], Jones, *et al*. [20], Jones, *et al*. [21]). Moreover, the use of a 1D velocity model (usually constructed from sonic log

data) in the downhole geometry may lead to an ambiguous 180° solution such that the source can be located on either side of a station, even after using this limitation. This 180° problem mainly occurs if the source depth lies in the middle of the geophone array. In contrast, monitoring systems using surface geophones do not suffer this ambiguity.

In this study, the modified procedure from Jones, *et al.* [21] for locating the hypocenter using the analysis of P-wave polarization was applied in constraining the event source. The 180° ambiguity was removed by adding a combination of polarity analysis to the routine data processing, as proposed by Havskov & Ottemöller [22]. Then, we located the hypocenter using a guided grid-search method. A simpler procedure is described briefly in Ry, *et al*. [23]. Also, the uncertainty ellipsoids of the location were calculated to estimate precision, accuracy, and ambiguity. It was shown that this location procedure could overcome the ambiguity problem due to the use of a near-vertical borehole array. Furthermore, the seismic source attributes of each microseismic event are defined by its moment magnitude. Brune's model [24] was implemented to estimate seismic moment and moment magnitude.

Important geomechanical parameters of the reservoir can be derived based on the results of the microseismicity distribution and the source attributes. However, induced seismicity (in which the injection directly causes fractures) has to be distinguished from triggered seismicity (in which the injection accelerates pre-existing fractures). The distribution of the induced seismicity allows a preliminary estimation of the stimulated reservoir volume (SRV) and orientation of fractures (see e.g. Rodriguez-Pradilla [25]). Meanwhile, triggered seismicity can be generated if any fault is near to rupture and may cause an earthquake. As a precaution, this needs to be considered by analyzing the magnitude of microseismicity. Our results showed that both induced and triggered seismicity may occur close to the area of hydraulic-fracturing treatment.

2 Case Study

The study region lies within the onshore portion of the Tertiary Kutai Basin on the eastern margin of the island of Kalimantan, Indonesia, encompassing four large to enormous hydrocarbon accumulations: the Mutiara, Semberah, Nilam, and Badak fields and also several other smaller fields, as noted by McClay, *et al*. [26]. The study area is located in Pamaguan field, one of the smaller fields and part of the Lower Kutai Basin. Coal-bed methane (CBM) gas is presumed to be located in the coal seams within the Balikpapan formation. The Balikpapan formation was deposited in the middle Miocene and is composed of

sub-bituminous coal seam interbedded with quartz sandstone and shaly claystone, and is about 800 m thick.

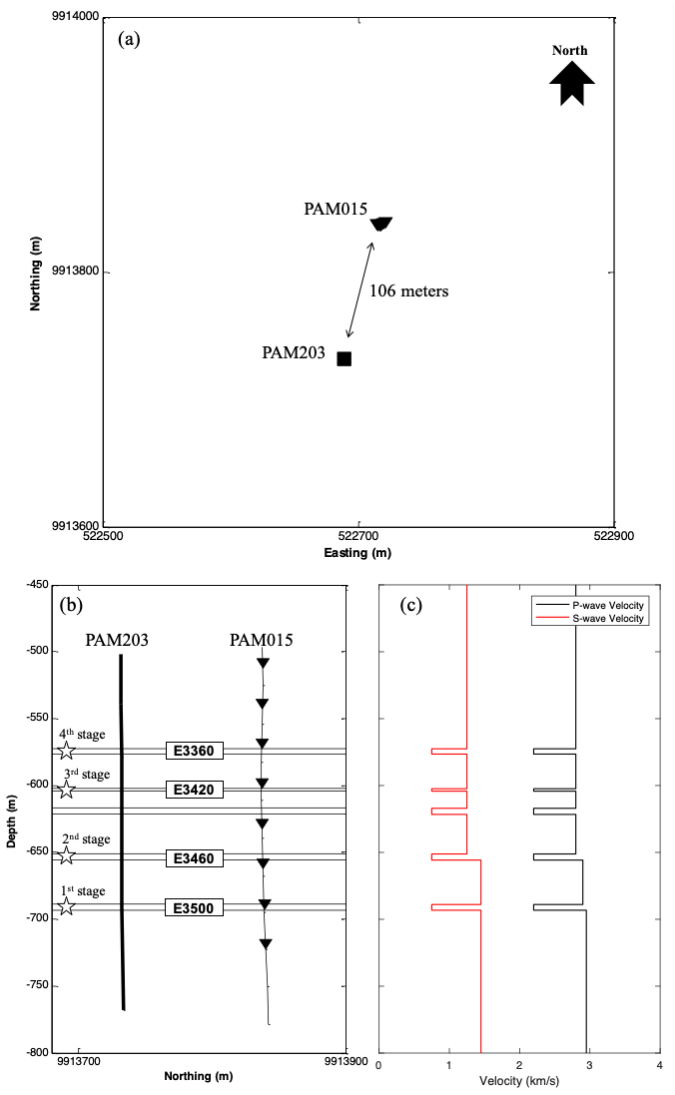

Figure 1 (a) Map of study array at the CBM field showing PAM203, the treatment well, and PAM015, the monitoring well. (b) The geometry of the treatment well and the borehole seismometers (in the northing cross section): E3360, E3420, E3460 and E3500 are interbedded coal seams; the locations of the injection stages and recorders are indicated by stars and triangles, respectively. (c) The one-dimensional velocity model for P- and S-waves was derived from sonic logs recorded for this study.

Two wells were drilled in the study area, PAM015 and PAM203 (Figure 1(a)). In 2012, a multistage hydraulic-fracturing was conducted in the PAM203 well, while the monitoring stations were installed in the PAM015 well. The objectives were to stimulate flow, develop a fracture network and increase the reservoir's permeability. There were four injection stages in the treatments, where each operation was performed on different coal seams at various depths – varying between 560 and 700 m. The locations of the injection stages, which took place on 28 July, 2 August, 9 August, and 14 August 2012 respectively, are shown in Figure 1b. The coal seams E3360, E3420, E3460, and E3500 were interbedded with sandstone, corresponding to the Balikpapan formation, and each coal seam had a thickness of around 2-5 m.

The microseismicity related to this fracturing was monitored using a single downhole-seismic acquisition system composed of eight 3-component seismometers. The eight seismometers were installed in a near-vertical array in the PAM015 well with a depth interval of 30 m (Figure 1(b)). The deployment of this system allowed the acquisition of 24-hour seismic records a day in real time, with a sampling interval of 0.25 ms, resulting in a bandwidth frequency between 15 and 2000 Hz.

The one-dimensional blocked velocity model was derived from sonic logs acquired in the PAM203 well, i.e. the treatment well (Figure 1(c)). Every velocity block delineates a lithology group and is assumedly valid for the whole study area. The thinly layered blocks of low velocity represent coal seams in which the CBM gas is presumed to exist. The other blocks represent background lithology associated with sandstone.

3 Location of Microseismic Events

Microseismic processing to locate an event hypocenter consists of 3 main steps. It should begin with picking an accurate arrival time for the P- and S-wave phases. After that it is necessary to estimate the back azimuth to the source in order to confine its location by analyzing the P-wave polarization. In addition, the 180° ambiguity is removed by analyzing the polarity of the P-waves' first motion. Lastly, the hypocenter location is constrained through a guided inversion process in grid-searching.

3.1 Arrival Time Picking

Pavlis [15] notes that an error in arrival time picking would contribute greatly to location inaccuracy. Therefore, this initial step must be carefully considered because it determines all of the following processes. In general, phase arrival times are manually picked. However, working on large data sets makes manual

picking very time-consuming. In order to overcome the problems of consistency and human resources, according to Earle & Shearer [27], an automatic procedure can be carried out for arrival time picking by comparing a short-term average and a long-term average of the signal. Then, the time picked is assigned to a value with regard to previously set thresholds. Jones, *et al.* [20] state a drawback of such an automatic procedure, which is less consistency in where the pick is placed concerning the waveform, e.g. first break or peak and trough. Recently, an iterative semi-automatic picking procedure based on stacked pilot traces and cross-correlation has been introduced to reduce errors in phase picking (Rowe, *et al.* [28], de Meersman *et al.* [18]). However, Sharma, *et al.* [29] emphasize that no time-picking algorithm is optimal under all conditions, especially under noisy conditions, and thus understanding the parameters and limitations is necessary (Akram and Eaton [30]).

In this study, 1864 microseismic events were identified from all injection stages. A combine semi-automatic picking procedure was used. The arrival times for all P- and S-phases were picked manually. After this very time-consuming step, a refinement of the picks was performed to reduce human errors and misidentification. The time picks were refined using the modified energy ratio (MER) algorithm to acquire highly consistent picks. This algorithm is an expansion of the short-time average and long-time average approach, which has equal size of the pre- and post-sample windows. The modification is made to estimate the energy ratio between noise and signal more appropriately. Akram and Eaton [30] defined the MER value at the *i*-th time sample as:

$$MER(i) = \left(\frac{\sum_{j=i}^{i+w} x_j^2}{\sum_{j=i-w}^{i} x_j^2}\ |x_i|\right)^3 \tag{1}$$

where w is the window length, and x is the input series. This energy ratio function is sensitive to any shift between two different wave phases (e.g. noise to P-phase, or P-phase to S-phase) and consequently the time concordance linked to the maximum MER value is the representative pick of the first break.

The information from the initial time picks can be used to restrict the sample area for calculating the MER. Figures 2(a-c) show the refinement of phase picking of the P- and S-waves with a high signal-to-noise ratio (SNR). It can be seen that the refined picks are placed on the first break of the signal better than those from manual picking. With or without the restricted sample area (Figures 2(b) and 2(c)), the MER value is maximal at the same time pick. However, a problem occurs if the recorded waveform has a low SNR, as shown in Figures 2(d-f). The maximum MER value is different between the restricted sample area (Figure 2(e)) and the unrestricted sample area (Figure 2(f)). The refined picks according to the restricted sample area are placed better on the first break. From this comparison, it can be seen that limitation of the sample area based on a

priori information is fundamental to accommodating all waveforms with different SNRs.

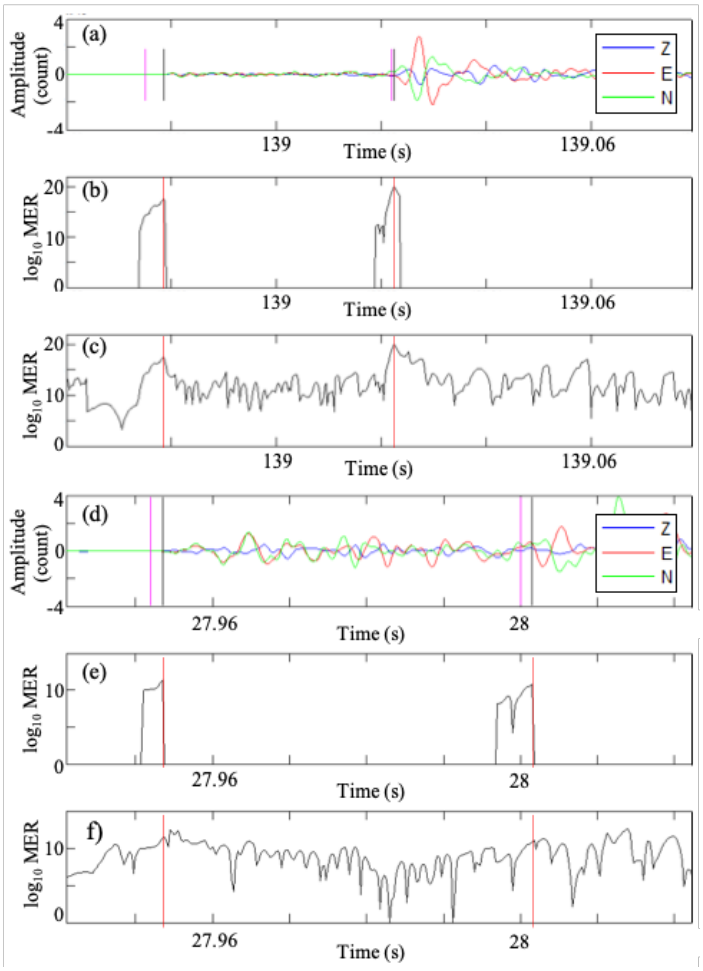

Figure 2 (a) Instance of 3-component signals with high S/N ratio for arrival time picking of P- and S-phases (first signals). Magenta and black lines show manual and refined picks, respectively. (b) MER response curve of first signals with a restricted sample window. (c) MER response curve of first signals without a restricted sample window. Red dashed-lines indicate the refined arrival times. (d) Example of 3-component signals with typical S/N ratio for arrival time picking of P- and S-phases (second signals). Magenta and black lines depict manual and refined picks, respectively. (e) MER response curve of second signals with a restricted sample window. (f) MER response curve of second signals without a restricted sample window. Red dashed-lines indicate the refined arrival times.

3.2 Estimation of Back Azimuth

We must estimate the back azimuth of every single event that describes the course from the receiver to the event source. This is required because single near-vertical borehole geometry could lead to ambiguity of the location solution in the horizontal direction; it can be done by analyzing the polarization. Since the P-wave is polarized vertically and radially, its vector of particle motion is utilized to estimate the back azimuth.

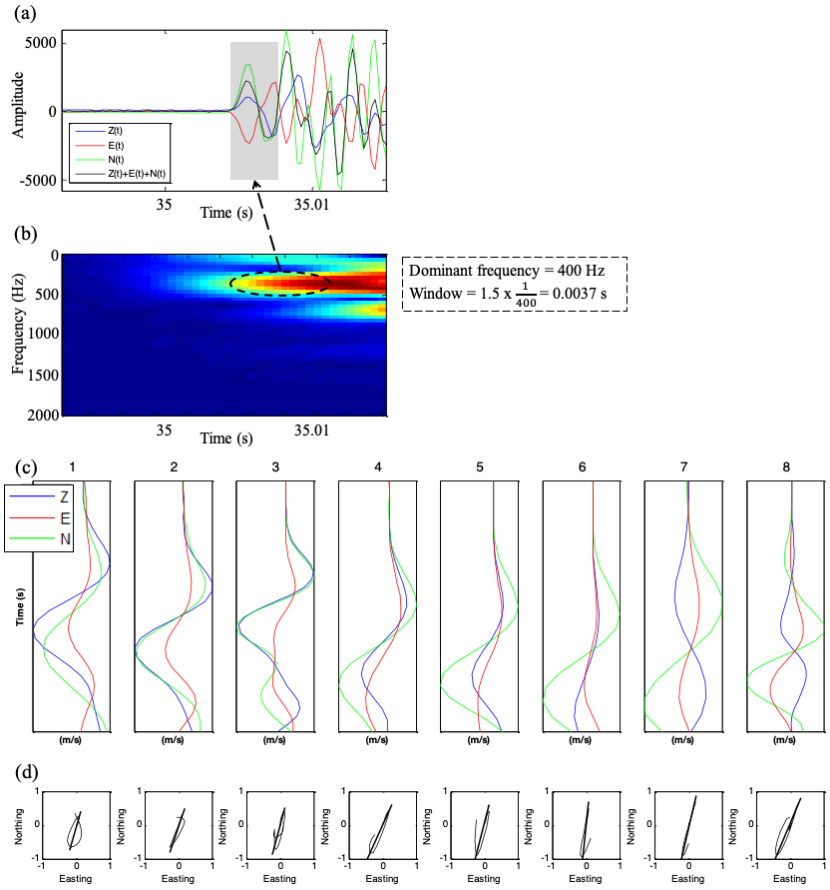

Figure 3 Instance of P-wave polarization analysis: (a) the observed 3-component signals and the stack of amplitudes. The grey window shows the windowing of the very first arriving P-wave based on time-period analysis; (b) spectrogram of the stack of signal amplitudes that provides the information of the dominant time-period; (c) the selected waveforms from 8 monitoring stations; and (d) hodograms of the horizontal components (the black line shows the cross-plotting and the bold black line shows the principal direction) for all monitoring stations that recorded the same event.

First, a P-wave signal is windowed at the very first part after it arrives at a receiver to gain a clear linear polarization (see Figure 3(a)). In this selection, the window length used was 1.5 multiplied by the dominant time-period of a single signal. This length will be different for each station and each event. In other words, if we have a signal consisting of a dominant time-period of 1.34 ms, it means that the signal will be cut from the time it arrives until 2 ms afterward. The dominant frequency can be calculated for example by short-time Fourier transform (STFT). The spectrogram of the stack of signal amplitudes containing the information of the dominant time-period is given in Figure 3(b).

Table 1 Combination of Polarities in Correcting Polarization Azimuth*

For up-going wave									For down-going wave								
Z	+	-	+	-	+	-	+	-	Z	+	-	+	-	+	-	+	-
N	+	+	-	-	-	-	+	+	N	+	+	-	-	-	-	+	+
E	+	+	+	+	-	-	-	-	E	+	+	+	+	-	-	-	-
Add	180	0	0	180	0	180	180	0	Add	0	180	180	0	180	0	0	180

* Modified from Havskov and Ottemöller [22] to accommodate down-going wave.

Furthermore, the principal components of polarization for the selected P-wave signals were estimated. Following de Meersman, *et al.* [31], the data covariance matrix was calculated for the selected signal using analytical signals of three-component data. The real parts of the first eigenvectors (A_N for the north-south component, A_E for the east-west component, A_Z for the vertical component), decomposed from the analytical signals, are the principal components. As vectors, these principal components can be derived into the principal signal direction and the polarization azimuth.

Then, the P-wave polarization was depicted in a cross-plot hodogram of the particle motion on the east-west and north-south components (Alessandrini [16], Moriya [17]). For instance, Figure 3(c) shows all windowed signals from 8 monitoring stations and their hodograms of the horizontal components, as shown in Figure 3(d), represent the polarized ground motions and the principal directions in graphics.

Finally, the signal polarization azimuth ∅ is given by Havskov and Ottemöller [22] as follows:

$$\emptyset = arctan\frac{A_E}{A_N} \tag{2}$$

As a consequence of the limitation of arctangent solutions, the signal polarization azimuth ∅ is limited by:

$$-90 \leq \emptyset \leq 90 \tag{3}$$

Regarding this limitation, there is an ambiguity of 180° in this solution. Determining the back azimuth based on this solution would lead to a wrong location; for example, the source could be located on either side of a receiver. For obtaining the actual back azimuth of the event, we need to add a correction to the signal polarization azimuth. Given by Havskov and Ottemöller [22] in observing the first polarities of the P-waves, when the first motion is upward on any instrument component, then its radial motion is directed away from the source. If the first motion is downward, the opposite is true. Therefore, in order to correct the back azimuth, the fact can be used that the first P-wave polarities could either be positive or negative in a combination of all three-components. This combination of polarities and its impact on the correction are shown in Table 1.

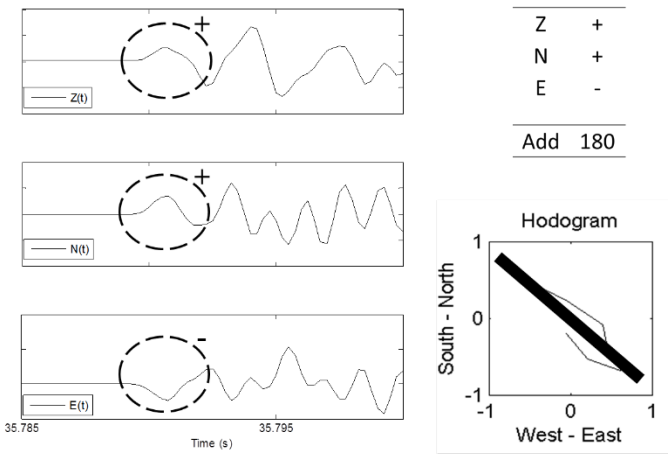

Figure 4 Illustration of polarity review for removing 180° ambiguity.

An illustration of the polarity review for removing 180° ambiguity is given in Figure 4. Here, the first polarities for all components in a station are defined. The polarities are positive, positive and negative for the vertical, N-S, and E-W components respectively. After obtaining the initial information, the source is located below the monitoring station. Calculating its P-wave polarization, the obtained back azimuth is -48° or 312°. However, according to Table 1, 180° must be added to the solution. Therefore, the back azimuth from the station to the source is 132°.

In the end, the same calculation needs to be done for all receivers that have recorded the same event for obtaining their respective back azimuth values. Then, the final back azimuth to the event source is defined as a weighted

average of all those values. A receiver located closer to the event, marked by a faster arrival time, will have a higher weight in the averaging.

3.3 Locating

Using the inputs gained from the two previous steps, the last step is to constrain the hypocenter of the microseismic events. This involves an inversion process using guided grid-search for producing an accurate solution. According to Jones, *et al.* [21], the model space can be limited to guide the grid-search in the trace area in the direction of the source using the information of the back azimuth. The grid-search optimization technique works to minimize the misfit function by seeking systematically through all spots in the model space that has already been set. In general, the misfit function is defined as the difference between observed and calculated arrival times for all P- and S-phases that have been identified in some of the stations.

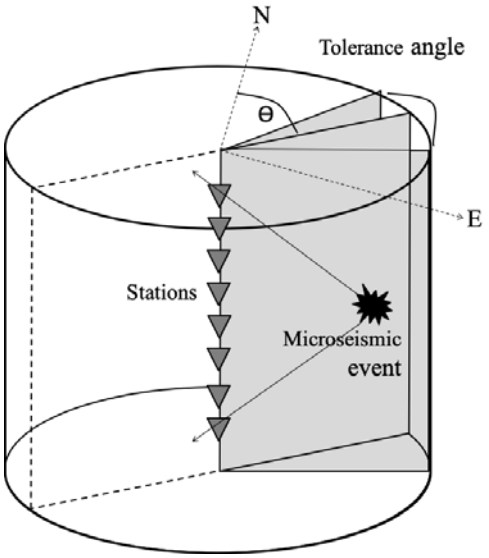

Figure 5 A schematic illustration showing the connection between the radial symmetry and the confined area of grid-searching from the monitoring stations (gray zone) limited by the back azimuth and tolerance angle.

In practice, even after obtaining the time picks of the first break, the event's origin time is still unknown. The origin time of an event must be solved upon the locating inversion and therefore optimization is usually more difficult. To be able to calculate it separately from the optimization, the master station approach is applied (Zhou [32], Jones, *et al.* [21]), which minimizes the differential merger between observed arrival times and their correlated calculated travel

times. The misfit function in the minimization of all combinations of arrival times and sensors is given by:

$$E(i) = \sum_{j=1}^{N-1} \sum_{k=1+1}^{N} \left[\left(t_j^{obs} - t_k^{obs} \right) - \left(T_{ij}^{cal} - T_{ik}^{cal} \right) \right]^2 \quad (4)$$

which is generalized as an objective function. In Equation (4), t_j^{obs} is the observed arrival time at receiver *j*; t_k^{obs} is the observed arrival time at receiver *k*; T_{ij}^{cal} is the calculated travel time from source *i* to receiver *j*; and T_{ik}^{cal} is the calculated travel time from source *i* to receiver *k*.

The use of the master station method allows us to calculate the origin time after the inversion. The origin time can be computed by averaging the differentials of the observed arrival times and the calculated travel times from the best-fit model. It can be expressed as follows:

$$\tau_i = \left| \frac{1}{N} \sum_{j=1}^{N} (t_j^{obs} - T_{ij}^{cal}) \right| \quad (5)$$

Grid-search optimization techniques usually suffer from the intersection between computational time and resolution. However, the information of the back azimuth to the source is powerful in significantly reducing the model search space. Jones, *et al.* [21] mention that the radial symmetry between the downhole array and the laterally extending 1D vertical velocity model enables the decoupling of the polarization direction and travel time minimization. Hence, the reduction in the spatial parameters makes a simple grid-search an appealing possibility and this simplification also sustains high-resolution models in dense grid-spacing, smaller than 1 m in spatial distance. Figure 5 shows the back-azimuthally confined area of grid-searching starting from the downhole stations. To get more sample data and tolerate some uncertainty of the particle motion results, the searching area was widened by ± 5° of tolerance angle with respect to the back azimuth (see Figure 5). The inversion was performed in Cartesian coordinates (x,y,z).

4 Moment Magnitude

Brune's model [24] was implemented to calculate the moment magnitude M_w of the microseismic events. This model applies to all types of earthquakes (local, regional and teleseismic) and seismic events of any size (micro, small, medium and large magnitudes) and allows an estimation of the source radius and stress drop (Rodriguez-Pradilla [25]). Moment magnitude is defined as:

$$M_w = \frac{2}{3} \log M_0 - 6.07 \quad (6)$$

M_0 is the seismic moment in Newton meters. It can be calculated by fitting the frequency spectrum of displacement of a seismic signal to the theoretical source spectrum $S_0(f)$ of Brune's model [24], which is defined as:

$$S_0(f) = \frac{\Omega_0}{[1+(f/f_c)^{\gamma n}]^{1/\gamma}} \quad (7)$$

where Ω_0 is the long-period amplitude, f_c is the corner frequency, n = 2, and γ = 2 is the high-frequency source-spectral roll-off, according to Mukuhira, *et al.* [33].

The first step is to obtain Ω_0 and f_c for each microseismic event by applying spectral fitting. To begin with, for a single event, the P phase of each recording station was windowed from a seismic trace. The seismic trace is adjusted after instrument correction to obtain the ground displacement in meters. For downhole observation, the P wave is not always necessarily dominant in the vertical component; it can also be in the horizontal components (N-S and E-W). Therefore, the seismic trace for windowing should be selected from a component where its P-wave trace has the highest signal-to-noise ratio. After acquiring the windowed seismic trace, Fourier analysis is applied to calculate its frequency spectrum (Figure 6). Then, the theoretical source spectrum (Equation 7) is fitted to the frequency spectrum by a least-squares regression to obtain optimum Ω_0 and f_c (Figure 6). This calculation must be repeated for each receiver. Furthermore, the same procedure has to be applied for the S phase.

Once both Ω_0 and f_c have been obtained from the spectral fitting, the seismic moment M_0 for each receiver and each phase (P and S) can be calculated (Brune [24]):

$$M_0 = \frac{\Omega_0 4\pi\rho V^3 R}{F_R} \quad (8)$$

where ρ is density (ρ = 1.3 g/cm^3 for events in the stimulated coal seam; ρ = 2.3 g/cm^3 for events in other locations), V is the velocity of the phase being modeled in meters per second, R is the distance from source to receiver in meters (calculated by ray tracing), and F_R is the radiation pattern. According to Boore and Boatwright [34], the average radiation pattern coefficient can be defined as F_α = 0.52 for the P-wave and F_β = 0.63 for the S-wave, if the focal mechanism is unknown.

The use of the average radiation-pattern correction in the estimation needs to be considered. Maxwell [1] explains that if magnitudes are being estimated for the downhole array using only one phase (e.g. P) especially, the average value is likely to overestimate or underestimate the radiation. However, if magnitudes or seismic moments are computed separately for both P- and S-waves and then

averaged, any uncertainty or error associated with unknown radiation patterns needs to be compensated because the nodal plane of one phase conforms to the maximum of the other phase.

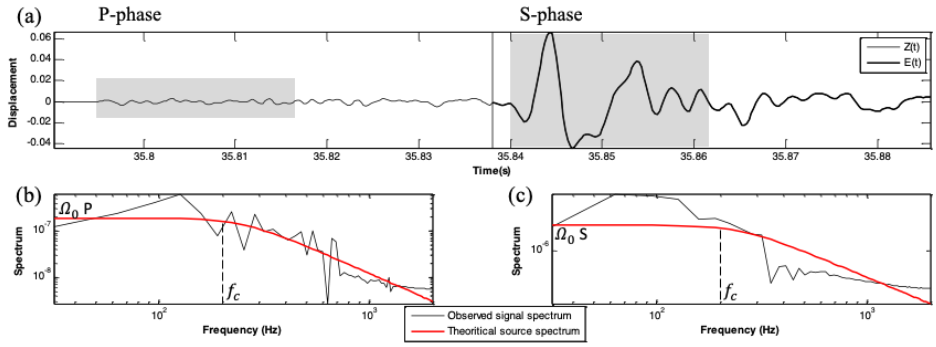

Figure 6 (a) Seismic trace after instrument correction. Gray windows show the windowed P phase and S phase, respectively. (b) Spectral fitting of the Brune's model source spectrum (red line) for the signal spectrum of the P-phase window (black line), and (c) for the signal spectrum of the S-phase window (black line). The corner frequency for both phases has the same value.

5 Results and Discussion

We have successfully located 1864 microseismic events associated with the four injection stages using guided grid-search (Figure 7(a)). Generally, the microseismic events occurred at depths where the injections were performed on a coal seam (Figure 1(b)). Meanwhile, the uncertainty of the hypocenters ranged from 5 to 10 m. However, the confidence ellipse of every event location was mainly elongated within its cluster and thus misinterpretation was avoided, because any error of location would still yield a solution within the cluster. In every stage, the depths of the events are well correlated with the location of the fracturing operation. The hypocenters were distributed with RMS misfit varying between 0.1 and 10.0 ms (Figure 7(b)). Figure 7(c) depicts the histograms of travel-time residuals for the P and S phases. Notice that the P phase gave a better distribution of travel-time residuals than S. Both RMS misfit and the uncertainty distribution were used as evidence that the inversion result is reliable. The critical geomechanical parameters of the reservoir can be derived using this result.

An intriguing feature occurred in the third injection stage and therefore our discussion will be focused on the microseismic events related to this stage. The third stage was conducted on 9 August 2012 and consisted of two fracturing injections. The first injection was a mini-frac consisting of 530 BBL of KCL

with an injection rate of 18 BPM, while the second injection was propped fracturing consisting of 1500 BBL of KCL with an injection rate of 18 BPM. Both injections were targeted on the second thin layer of the coal seams, i.e. E3420 (Figure 1(b)). Between 9 and 11 August 2012, 1584 microseismic events were identified, contributing 85% of the total recorded events. The third stage dominated the stimulation of microseismic events in these operations (see Figure 8).

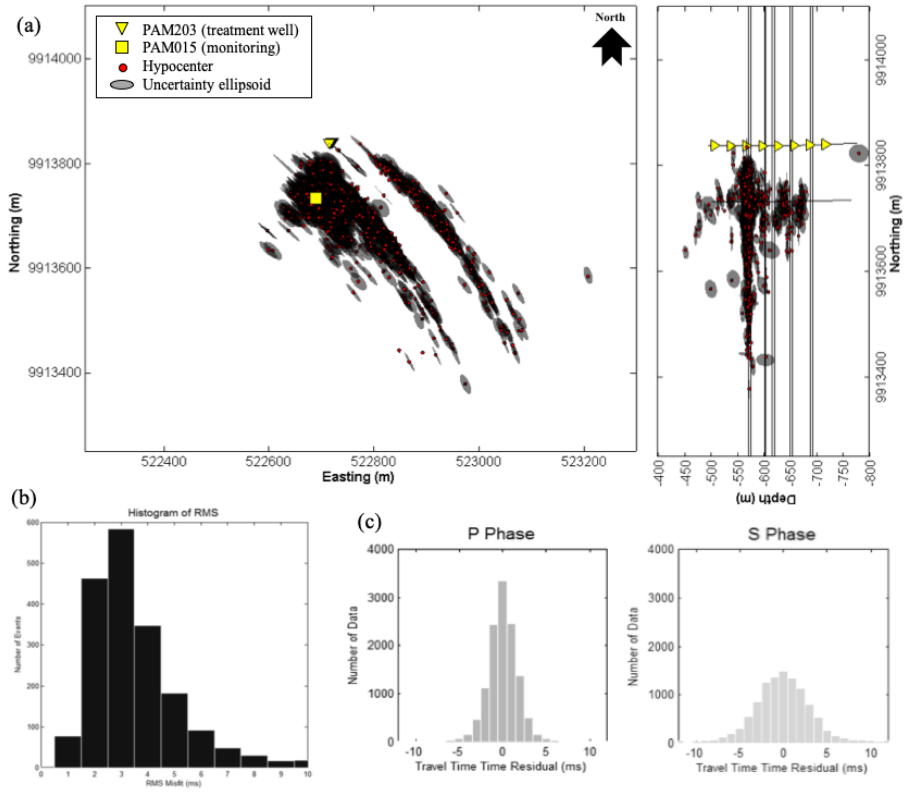

Figure 7 (a) Map of observed microseismic events (red dots) at the CBM field under study after four stimulations stages. (b) Histogram of RMS misfit of the inversion for locating the events. (c) Histograms of travel-time residuals for the P and S phases.

After the third stage of the injection operation, the depths of the events seemed to correspond well with the thickness of the stimulated coal seams (Figure 8(a)). The injections were targeted on coal seam E3420 (Figure 1(b)), but in fact most of the events occurred on E3360, the top coal seam. It can be inferred that the generated fractures were confined to both coal seams, E3420 and E3360. It is

possible that coal seam E3360 was much weaker than E3420. Therefore, even though the stimulation was located on E3420, the fractures developed on E3360. This experiment shows that fractures can be generated not only on a targeted coal seam but also on a nearby coal seam that is weaker and cracks easily. This needs to be considered carefully since it would be perilous if there is a water zone between the coal seams, which may leak into the reservoir and decrease the permeability significantly.

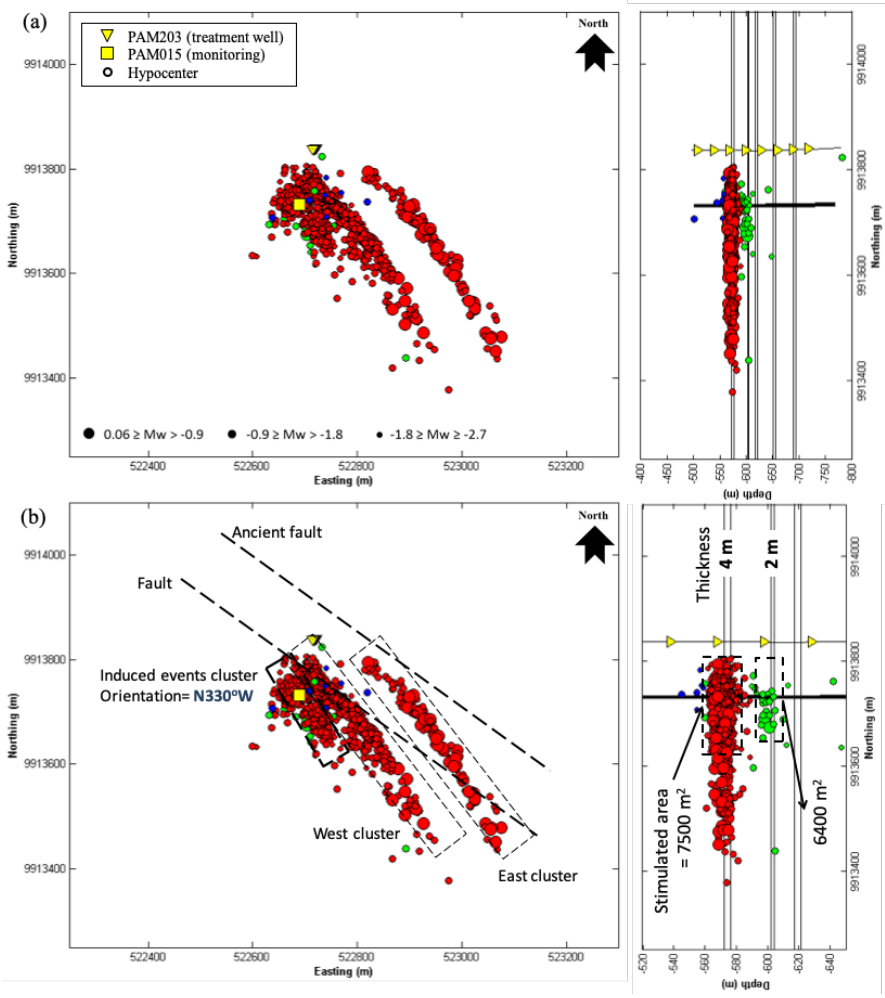

Figure 8 (a) Map of microseismic events at the CBM field under study stimulated by hydraulic-fracturing treatment after the third stage. The bubble scale represents the moment magnitudes of the events. (b) Interpretation of the clusters of the induced and triggered seismicity.

In our interpretation, the horizontal distribution of 1584 microseismic events is divided into 3 clusters: (i) induced events cluster, (ii) West cluster, and (iii) East cluster, as shown in detail in Figure 8(b). It is necessary to distinguish which clusters are associated with induced seismicity or triggered seismicity due to the differences in their features.

In the first cluster, the microseismic events spread in the N330°W direction starting from the treatment well. This cluster reasonably was well associated with the injections in the third stage. As induced seismicity, the fracture was directly caused by the injection. Despite the depth distribution, in this cluster fractures were generated around the treatment well. As more fluid was injected, the fractures continued to widen and grow outward from the well. Most of the fractures generated during hydraulic-fracturing followed the principal stress environment, causing an opening and a slip to get filled by proppant (Rodriguez-Pradilla [25]).

Near the first cluster, the microseismic events in the second cluster dispersed in the SE-NW direction close to the treatment well, with a length of approximately 500 m. The West cluster showed the existence of triggered seismicity, where the cracking of pre-existing fractures was accelerated by the injections but eventually would have occurred naturally. A previous study inferred that there is a fault in the SE-NW direction around the treatment well based on 2D seismic cross sections (Figure 8(b)). As more fluid was injected and the fractures grew outward from the well, the pre-existing fault was stimulated, causing a slip in the fault. However, an important question is whether the fracture in this fault is still being opened or not. There is no evidence of a connection between this cluster and the injected propped fluid and therefore without the proppant the fractures can be assumed to close right after they opened. It is a concern that the triggered seismicity is an undesired activity, therefore considerable precautions need to be taken, e.g. by monitoring the magnitude of microseismic events.

Meanwhile, the East cluster in any case had the most interesting distribution. As the second cluster, it is associated with triggered seismicity. The microseismic events elongated in the same direction, parallel to the West cluster. However, there is a gap that separates these two clusters. The previous study using 2D seismic cross-sections deduced an existing ancient fault around that area (Figure 8(b)). In his study, Maxwell [1] claims that triggered seismicity may occur if a fault is close enough to failure and requires comparatively less pressure change to cause an earthquake. How close ‘close enough’ is, is not explained in detail. Comparing the magnitudes, the East cluster consisted of events that had relatively higher magnitudes. We interpret these growing magnitudes as a proof of re-activation of the ancient fault. It can be inferred that a larger event at a certain distance may be re-activated as a result of hydraulic fracturing.

Therefore, ample precautions are necessary. In this study, the magnitudes of the East cluster events can still be considered small, but they nevertheless still point at the importance of microseismic monitoring.

Lastly, our results showed that the first cluster was the only indicated induced seismicity. The distribution of the induced seismicity events allows a preliminary estimation of the stimulated reservoir volume (SRV) and orientation of the fractures. The SRV value was calculated by assuming that the entire fractured area and the entire coal seam thickness were stimulated effectively. Since two coal seams were stimulated, the SRV was defined as the multiplication of thickness and fractured area. Owing to the third stage, the SRV value from E3420 (fractured area = 6400 m^2, thickness = 2 m) was 12,800 m^3 and the SRV value from E3360 (fractured area = 7500 m^2, thickness = 4 m) was 30,000 m^3; hence the total SRV was 42,800 m^3. Furthermore, the orientation of stimulated fractures was N330°W.

6 Conclusion

It was successfully demonstrated that microseismic monitoring using a single near-vertical borehole requires a great deal of attention in the data processing, especially for locating events. The locating procedure consists of 3 main steps, starting with accurate arrival time picking for both the P- and S-phases, the inclusion of P-wave particle motion for estimating the back azimuth, and the inversion process for determining the hypocenters. It is noted that the additional input on P-waves polarization is necessary to confine the direction from the monitoring stations to the event source and obtain an accurate source location. Despite the ambiguity problem, the location procedure that was applied in this study is reliable and robust for solving this ambiguity.

As a result, it is inferred that both induced and triggered seismicity may occur within the time of observation regarding hydraulic-fracturing treatment, so monitoring and distinguishing them is crucial. The seismic-source attribute, notably the magnitude of events, can be used as a separating indicator for the observed clusters. A cluster associated with triggered seismicity will have relatively bigger magnitudes than a cluster of induced events. Nevertheless, triggered seismicity can lead to inadvertant collapse and demands substantial disaster precautions, in particular for preventing re-activation of pre-existing faults.

Acknowledgements

The authors gratefully acknowledge Vico Indonesia and SKK Migas Indonesia for their permission to use the study data. We personally thank Ahmad Fanani

Akbar, Billy Prabowo, Hasbi Ash Shiddiqi, Rendy Delliansyah, and Wiku Widyoyudo for their assistance in the step of manual time picking. Thanks also go to the Indonesia Endowment Fund for Education (LPDP) for funding RVR's education during the course of conducting this study.

References

[1] Maxwell, S.C., *Microseismic Imaging of Hydraulic Fracturing: Improved Engineering of Unconventional Shale Reservoirs*, SEG Distinguished Instructor Series, (17), 2014. DOI:10.1190/1.9781560803164.

[2] Stimac, J., Nordquist, G., Suminar, A. & Sirad-Azwar, L., *An Overview of the Awibengkok Geothermal System, Indonesia*, Geothermics, **37**, pp. 300-331, 2008.

[3] Akbar, A.F., Nugraha, A.D., Sule, R. & Juanda, A.A., *Hypocenter Determination Using Simulated Annealing, Updated 1D Seismic Velocity Model, and Focal Mechanism Analysis*, AIP Conf. Proc., **1554**, pp. 285-289, 2013.

[4] Nugraha, A.D, Syahputra, A., Fatkhan & Sule, R., *Seismic Velocity and Attenuation Structures in the Geothermal Field*, AIP. Conf. Proc., **1554**, pp. 238-241, 2013. DOI:10.1063/1.4820329.

[5] Hasanah, M.U., Nugraha, A.D. & Sule, R., *Attenuation Tomography Using MEQ Data in the A Geothermal Field*, AIP. Conf. Proc., **1554**, pp. 273-276, 2013. DOI:10.1063/1.4820338.

[6] Ry, R.V. & Nugraha, A.D., *Reservoir Characterization around Geothermal Field, West Java, Indonesia Derived from 4-D Seismic Tomography*, IOP Conf. Series: EES, **29**(1), 2016. DOI:10.1088/1755-1315/29/1/012001

[7] Fattah, E.I., Nugraha, A.D. & Sule, R., *An Integrated Method 3D Velocity Model and Fuzzy Clustering for Fracture Characterization*, IOP Conf. Series: EES, **62**, 2017. doi:10.1088/1755-1315/62/1/012026.

[8] Rohaman, M., Suhendi, C., Ry, R.V., Prabowo, B.S., Widiyantoro, S., Nugraha, A.D., Yudistira, T. & Mujihardi, B., *The Preliminary Results of Gmstech: A Software Development for Microseismic Characterization*, IOP Conf. Series: EES, **62**, 2017. DOI:10.1088/1755-1315/62/1/012024.

[9] Palgunadi, K.H., Nugraha A.D., Sule, R. & Meidiana, T., *Steam and Brine Zone Prediction Around Geothermal Reservoir Derived from Delay Time Seismic Tomography and Anisotropy Case Study: "PR" Geothermal Field*, IOP Conf. Series: EES, **62**, 2017. DOI:10.1088/1755-1315/62/1/012027.

[10] Geiger, L., *Probability Method for The Determination of Earthquake Epicenters from Arrival Time Only*, Bull. St. Louis. Univ., **8**, pp. 60-71, 1912.

[11] Lienert, B.R., Berg, E. & Frazer, L.N., *Hypocenter: An Earthquake Location Method Using Centered Scaled and Adaptively Damped Least Squares*, Bull. Seism. Soc. Am., **76**(3), pp. 771-783, 1986.
[12] Nelson, G.D. & Vidale J.E., *Earthquake Locations by 3-D Finite Difference Travel Times*, Bull. Seism. Soc. A M., **80**(2), pp. 395-410, 1990.
[13] Lomax, A., Zollo, A., Capuano, P. & Vireux J., *Precise, Absolute Earthquake Location under Sommaevesuvius Volcano Using a New Three-Dimensional Velocity Model*, Geophys. J. Int., **146**(2), pp. 313-331, 2001.
[14] Ry, R.V. & Nugraha A.D., *Improve Earthquake Hypocenter Using Adaptive Simulated Annealing Inversion in Regional Tectonic, Volcano-Tectonic, and Geothermal Observation*, AIP. Proc. Conf., **1658**, 2015. doi:10.1063/1.4915012
[15] Pavlis, G.L., *Appraising Earthquake Hypocenter Location Errors: A Complete, Practical Approach for Single-Event Locations*, Bull. Seism. Soc. A M., **76**(6), pp. 1699-1717, 1986.
[16] Alessandrini, B., Cattaneo, M., Demartin, M., Gasperini, M. & Lanza, V., *A Simple P-Wave Polarization Analysis: Its Application to Earthquake Location*, Annali di Geofisica, **37**, 1994.
[17] Moriya, H., *Precise Arrival Time Detection of Polarized Seismic Waves Using the Spectral Matrix*, Geophysical Prospecting, **56**, pp. 667-676, 2008.
[18] De Meersman, K., Kendall J.M. & van der Baan M., *The 1998 Valhallmicroseismic Data Set: An Integrated Study of Relocated Sources, Seismic Multiplets, and S-Wave Splitting*, Geophysics, **74**(5), pp. B183-B195, 2009.
[19] Maxwell, S.C., Rutledge, J., Jones, R. & Fehler, M., *Petroleum Reservoir Characterization Using Downhole Microseismic Monitoring*, Geophysics, **75**(5), pp. 129-137, 2010.
[20] Jones, G.A., Raymer, D., Chambers, K. & Kendall, J.M., *Improved Microseismic Event Location by Inclusion of a Priori Dip Particle Motion: A Case Study from Ekofisk*, Geophysical Prospecting, **58**(5), pp. 727-737, 2010.
[21] Jones, G.A., Kendall, J.M., Bastow I.D. & Raymer D., *Locating Microseismic Events Using Borehole Data*, Geophysical Prospecting, **62**, pp. 34-49, 2013.
[22] Havskov, J. & Ottemöller L., *Routine Data Processing in Earthquake Seismology: With Sample Data, Exercises and Software*, Springer, 2010. DOI:10.1007/978-90-481-8697-6.
[23] Ry, R.V., Septyana, T., Widiyantoro, S., Nugraha, A.D. & Ardjuna, A., *Improved Location of Microseismic Events in Borehole Monitoring by Inclusion of Particle Motion Analysis: A Case Study at A CBM Field in*

Indonesia, IOP Conf. Series: EES, **62**, 2017. DOI:10.1088/1755-1315/62/1/012025

[24] Brune, J., *Tectonic Stress and the Spectra of Shear Waves from Earthquakes*, Journal of Geophysical Research, **75**(26), pp. 4997-5009, 1970.

[25] Rodriguez-Pradilla, G., *Microseismic Monitoring of a Hydraulic-Fracturing Operation in A CBM Reservoir: Case Study in The Cerrejón Formation, Cesar-Ranchería Basin, Colombia*, The Leading Edge, **34**(8), pp. 896-902, 2015. DOI:10.1190/tle34080896.1.

[26] McClay, K., Dooley, T., Ferguson, A. & Poblet, J., *Tectonic Evolution of the Sanga Sanga Block, Mahakam Delta, Kalimantan, Indonesia*, AAPG Bulletin, **84**(6), pp. 765-786, 2000.

[27] Earle, P.S. & Shearer, P.M., *Characterization of Global Seismograms Using an Automated Picking Algorithm*, Bulletin of the Seismological Society of America, **84**, pp. 366- 376, 1994.

[28] Rowe, C., Aster, R., Phillips, W., Jones, R., Borchers, B. & Fehler M., *Using Automated, High-Precision Repicking to Improve Delineation of Microseismic Structures at the Soultz Geothermal Reservoir*, Pure and Applied Geophysics, **159**, pp. 563-596, 2002.

[29] Sharma, B.K., Kumar A. & Murthy, V.M., *Evaluation of Seismic Event-Detection Algorithms*, Journal Geological Society of India, **75**, pp. 533-538, 2010. DOI:10.1007/s12594-010-0042-8.

[30] Akram, J. & Eaton, D.W., *A Review and Appraisal of Arrival-time Picking Methods for Downhole Microseismic Data*, Geophysics, **81**, pp. Ks71-Ks91, 2016. DOI:/10.1190/Geo2014-500.1.

[31] de Meersman, K., van der Baan, M. & Kendall, J.M., *Signal Extraction and Automated Polarization Analysis of Multicomponent Ray Data*, Bull. Seism. Soc. A M., **96**, pp. 2415-2430, 2006.

[32] Zhou, H.W., *Rapid Three-Dimensional Hypocentral Determination Using a Master Station Method*, Journal of Geophysical Research, **99**(B8), pp. 15439-15455, 1994.

[33] Mukuhira, Y., Asanuma, H., Niitsuma, H., Häring, M. & Deichmann, N., *Estimation of Source Parameter of Microseismic Events with Large Magnitude Collected at Basel, Switzerland in 2006*, Geothermal Resources Council Transactions, **34**, pp. 407-412, 2010.

[34] Boore, D.M. & Boatwright, J., *Average Body-wave Radiation Coefficients*, Bull. Seism. Soc. A M., **74**, pp. 1615-1621, 1984.